PHYSICAL REVIEW A **110**, 023117 (2024)

Fluorescence-mediated postcollision interaction in x-ray photoionization of the Xe *K* edge

E. Pelimanni,[1,*] G. Doumy,[1] P. J. Ho,[1] S. Li,[1] D. Céolin,[2] R. Guillemin,[3] I. Ismail,[3] D. Koulentianos,[4,5]
T. Marchenko,[3] D. Peng,[3,6] R. Püttner,[7] M. Simon,[3] O. Travnikova,[3] N. Velasquez,[3]
A. Verma,[3] D. A. Walko,[8] L. Young,[1,9] and S. H. Southworth[1,†]

[1]*Chemical Sciences and Engineering Division, Argonne National Laboratory, Lemont, Illinois 60439, USA*
[2]*Synchrotron SOLEIL, l'Orme des Merisiers, Saint-Aubin, BP 48, 91192 Gif-sur-Yvette, France*
[3]*Sorbonne Université, CNRS, Laboratoire de Chimie Physique-Matière et Rayonnement, LCPMR, 75005 Paris, France*
[4]*Center for Free-Electron Laser Science, DESY, Notkestrasse 85, 22607 Hamburg, Germany*
[5]*Department of Physics, Universität Hamburg, Luruper Chaussee 149, 22761 Hamburg, Germany*
[6]*European XFEL, Holzkoppel 4, 22869 Schenefeld, Germany*
[7]*Fachbereich Physik, Freie Universität Berlin, Arnimallee 14, 14195 Berlin, Germany*
[8]*Advanced Photon Source, Argonne National Laboratory, Lemont, Illinois 60439, USA*
[9]*The James Franck Institute and Department of Physics, The University of Chicago, Chicago, Illinois 60637, USA*

(Received 17 June 2024; revised 31 July 2024; accepted 5 August 2024; published 30 August 2024)

Postcollision interaction (PCI) in near-threshold photoionization of the *K* shell of atomic Xe is investigated with hard-x-ray synchrotron radiation. Applying Auger electron spectroscopy, line-shape distortion is monitored in the K-$L_2 \rightarrow L_2M_{4,5}M_{4,5}$ decay channel, where the initial K-L_2 ($K\alpha_2$) x-ray-emission step mediates the emission of the two continuum electrons. The *K*-edge result is compared to similar data obtained on direct $L_2M_{4,5}M_{4,5}$ decay at the L_2 edge without x-ray-emission. It is found that the evolution of the PCI shift with excess photon energy is very similar at both edges, but a subtle decrease in the PCI shift is observable at the *K* edge due to the effect of the ultrafast x-ray emission step delaying the PCI energy exchange by a few attoseconds.

DOI: 10.1103/PhysRevA.110.023117

I. INTRODUCTION

In x-ray photoionization of an inner-shell electron, followed by Auger decay of the short-lived inner vacancy state, energy exchange can occur between the two continuum electrons through postcollision interaction (PCI) [1,2]. Quantum theory combines the electrons into a two-electron continuum wave function [3]; however, observables such as line-shape distortions and peak-position shifts can be modeled semiclassically [4–6]. Qualitatively, when the fast Auger electron passes the slowly propagating photoelectron, a sudden increase occurs in the ion's attractive potential (from +1 to +2) that the photoelectron must overcome, and effectively, its kinetic energy is reduced. The Auger electron correspondingly gains energy, as from its perspective the slow photoelectron provides additional screening over the ion potential.

Clearly, the strength of PCI is sensitive to the excess energy of the photon above the ionization potential (IP), being especially prominent in near-threshold ionization. Moreover, very near the threshold, photoelectron "recapture" to unoccupied Rydberg orbitals also comes into play [7,8]. As the photon energy is increased well above the IP, PCI eventually becomes negligible, and the observed electron (binding) energies converge to the nominal values typically probed in conventional photoelectron spectroscopy experiments. In an electron spectrum, PCI is reflected into shifted and asymmetric line shapes for both the photoelectron and the Auger electron. However, while a deep core hole formed in the photoemission process can have different decay channels (e.g., *K*-shell x-ray emission, *KLL* Auger decay, *KLM* Auger decay, etc.) so that the photoelectron line consists of a superposition of different line shapes and therefore different PCI shifts, the history of an Auger electron is well known and consists of a single line shape with a well-defined PCI shift. Therefore, the Auger electron is better suited for studying the PCI effect than the photoelectron by conventional electron spectroscopy, apart from using coincidence methods in which multiple electrons (and ions) are detected simultaneously [9,10].

In deep-inner-shell ionization, where the relaxation typically occurs through a decay cascade, PCI can reach over multiple sequential decay steps [9,11]. Moreover, the initial decay steps of deep vacancies are dominantly radiative, in which case the emission of the second electron and PCI are mediated by x-ray emission [11,12]. For rare gases, such "delayed" postcollision interaction was previously probed in Ar [9–11,13] and in Kr [12,14] in the ∼3.2- and ∼14.3-keV binding-energy regimes, respectively. In the present work, we investigate x-ray-emission-mediated PCI at the *K* edge of Xe at ∼34.6 keV. This deep $\mathrm{Xe}(1s^{-1})$ core hole decays on the ultrafast timescale with a lifetime of just $\tau_{1s} = 68 \pm 2$ as and has a strong fluorescence yield of $89.0\% \pm 1.0\%$ [15]. We consider here the K-L_2 channel, which leads to an intermediate $\mathrm{Xe}(2p_{1/2}^{-1})$ state that subsequently relaxes by Auger decay. A thorough discussion of the broad $\mathrm{Xe}(2p_{1/2}^{-1})$ decay spectrum upon direct *L*-shell ionization was given recently by Püttner *et al.* [16]. Although this spectrum is wholly subject

---

[*] Contact author: epelimanni@anl.gov

[†] Contact author: southworth@anl.gov

to PCI, as an exemplar case of the phenomenon, we probe here only the $L_2M_{4,5}M_{4,5}$ transitions into Xe($3d^{-2}$) final states at ∼3.7-keV kinetic energy. These particular transitions were selected based on their relatively high intensity and simple characteristics, allowing a straightforward peak analysis and quantification of PCI-related kinetic-energy shifts.

The qualitative scheme of the monitored process can be written as

$$\begin{aligned} \mathrm{Xe} + \gamma_i &\rightarrow \mathrm{Xe}(1s^{-1}) + e_1 \\ &\rightarrow \mathrm{Xe}(2p^{-1}) + e_1 + \gamma_f \\ &\rightarrow \mathrm{Xe}(3d^{-2}) + e_1 + e_2 + \gamma_f \\ &\rightarrow \cdots, \end{aligned} \tag{1}$$

where γ_i is the incident photon, γ_f is the emitted (K-L_2) photon, e_1 is the slow photoelectron, and e_2 is the measured fast Auger electron. The three dots at the end emphasize the fact that further decay steps will follow from the Xe($3d^{-2}$) state. In our analysis it is, however, not necessary to include these later transitions, apart from noting that the consequently finite lifetime of the ($3d^{-2}$) state is also reflected to the peak widths. The analysis is carried out by quantifying the kinetic-energy shift of the Auger peak as a function of the photon energy in the vicinity of the Xe K edge. To highlight the effect of the mediating x-ray-emission step to the PCI shift, the K-edge results are compared to similar data obtained directly at the L_2 edge. At the L_2 edge, the $L_2M_{4,5}M_{4,5}$ Auger channel remains the same, but the x-ray-emission step is absent. The process is

$$\begin{aligned} \mathrm{Xe} + \gamma_i &\rightarrow \mathrm{Xe}(2p^{-1}) + e_1 \\ &\rightarrow \mathrm{Xe}(3d^{-2}) + e_1 + e_2 \\ &\rightarrow \cdots. \end{aligned} \tag{2}$$

As we will discuss below, in the processes described in Eqs. (1) and (2) there is a different average time delay between the absorption of the photon and the emission of the Auger electron, so that different PCI-shift values are observed for the same excess energy.

II. EXPERIMENT

The Xe K-edge data were measured at the 7-ID beamline [17] of the Advanced Photon Source (APS), in Lemont, Illinois. Hard x rays were obtained from the beamline's 3.3-cm period undulator A and monochromatized using the third-order diffraction from a Si(111) double-crystal monochromator; the x-ray bandwidth is estimated to be ∼2.8 eV for photon energies of 34.40–34.74 keV. Lower-order diffractions were suppressed with two 25-μm Cu filters. The x-ray spot size was limited with $0.65 \times 0.65\,\mathrm{mm}^2$ (horizontal × vertical) slits and is assumed to be of comparable size at the interaction point. The electron spectra were recorded using a 200-mm-radius Scienta EW4000 hemispherical electron analyzer, with the focusing entrance lens oriented perpendicular to the propagation direction of the x-ray beam and parallel to the horizontal x-ray polarization axis. A gas cell with small entrance and exit apertures for the x-ray beam and a narrow exit slit for the electrons on the analyzer side was placed at the interaction point and kept at ∼1.3 mbar (1 torr) with a constant flow of Xe.

The Xe L_2-edge data were measured at the GALAXIES beamline [18] of the SOLEIL synchrotron in Saint-Aubin, France. The spectra were recorded with a Scienta EW4000 hemispherical electron analyzer similar to that used for the K-edge data installed in the same orientation with the entrance lens parallel to the x-ray polarization axis. A gas cell with a continuous flow of Xe was installed at the interaction point. The x-ray bandwidth was on the order of 0.58–0.75 eV for photon energies of 4.8–6 keV and 0.8–1.33 eV for energies of 6–10 keV.

The kinetic-energy scales for both K-edge and L_2-edge spectra were calibrated using previously reported experimental energies of selected transitions in the L_2-decay spectrum (Table I in Ref. [16], with a reported uncertainty of ±0.7 eV). The photon energy in the L_2-edge experiment at SOLEIL was calibrated to the Xe $2s \rightarrow 6p$ resonance at 5451.37 eV [16] and should be accurate to $\lesssim 1$ eV. The photon energy in the Xe K-edge measurements at APS was calibrated to the first absorption maximum in the Ni K edge at 8331.49 eV [19]. We note that while this calibration was done using the first-order Si crystal diffraction in the monochromator, the Xe data were measured using the third-order diffraction, which may induce a small offset. The uncertainty of photon-energy calibration at the Xe K edge in the absolute scale is expected to be on the order of 2–4 eV. The photon-energy calibration in the relative scale (excess energy above the IP), which is relevant for the PCI analysis, was, however, determined separately from the measurement of the Xe K-edge threshold region and results in a lower uncertainty (see Fig. 3 and related discussion below).

III. RESULTS AND DISCUSSION

The Xe $1s$ photoelectron spectrum is shown in Fig. 1, reflecting the first step of the interaction at the K edge. The photon energy is more than 500 eV above the IP, so no significant PCI distortion is present. Data are shown at two different gas-cell pressures, 0.7 mbar (0.5 torr) and 1.3 mbar (1 torr), along with a Voigt line-shape fit applied to the former. The result is very similar to that in previous reports [15,20]. A somewhat arbitrary set of four peaks with profiles identical to the main line is used to account for the shake-up and -off contribution on the lower-kinetic-energy side [15] since the true underlying subpeak structure (consisting mainly of $5p \rightarrow 6p, 7p, \ldots,$ continuum excitations [15]) is not resolvable in detail. The slightly higher intensity in the satellite region in the higher-pressure measurement suggests that inelastic scattering of the photoelectrons from other xenon atoms likely has a small effect there as well (such contributions have been observed in the satellite region of the Ar $1s$ photoelectron spectrum [21,22]), but the dominant contribution should still come from the satellites [15]. Likewise, for the Auger spectra discussed below, we assume that a slight inelastic scattering contribution has no practical effect on the PCI analysis. The fitted Xe($1s^{-1}$) lifetime width (FWHM) is 10.0 ± 0.5 eV, which is comparable to the value of 9.6 ± 0.2 eV reported earlier [15]. Note that the Gaussian component extracted from the fit, reflecting the experimental resolution, is much smaller, around 5.3 eV.

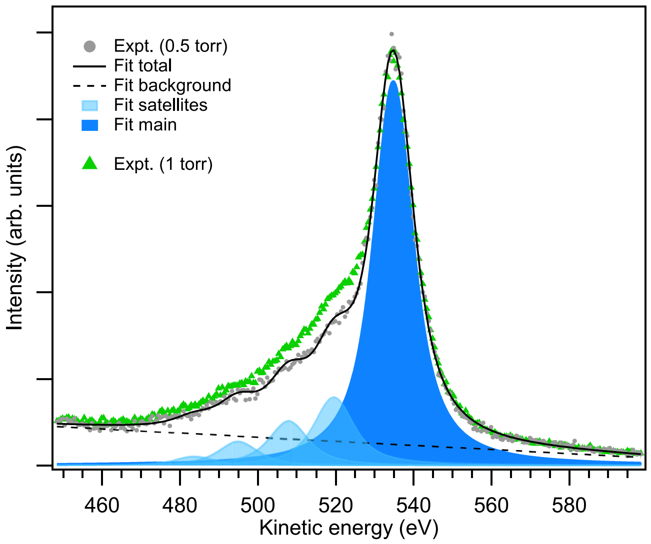

FIG. 1. Experimental Xe 1*s* photoelectron spectra measured with a photon energy of 35 098 eV. Two spectra are shown, measured at 0.7 mbar (0.5 torr) with one 25-μm Cu filter and at 1.3 mbar (1 torr) with two 25-μm Cu filters. The 0.7-mbar measurement is fitted with a series of Voigt profiles accounting for the main ($1s^{-1}$) line as well as for the shake-up and -off satellites.

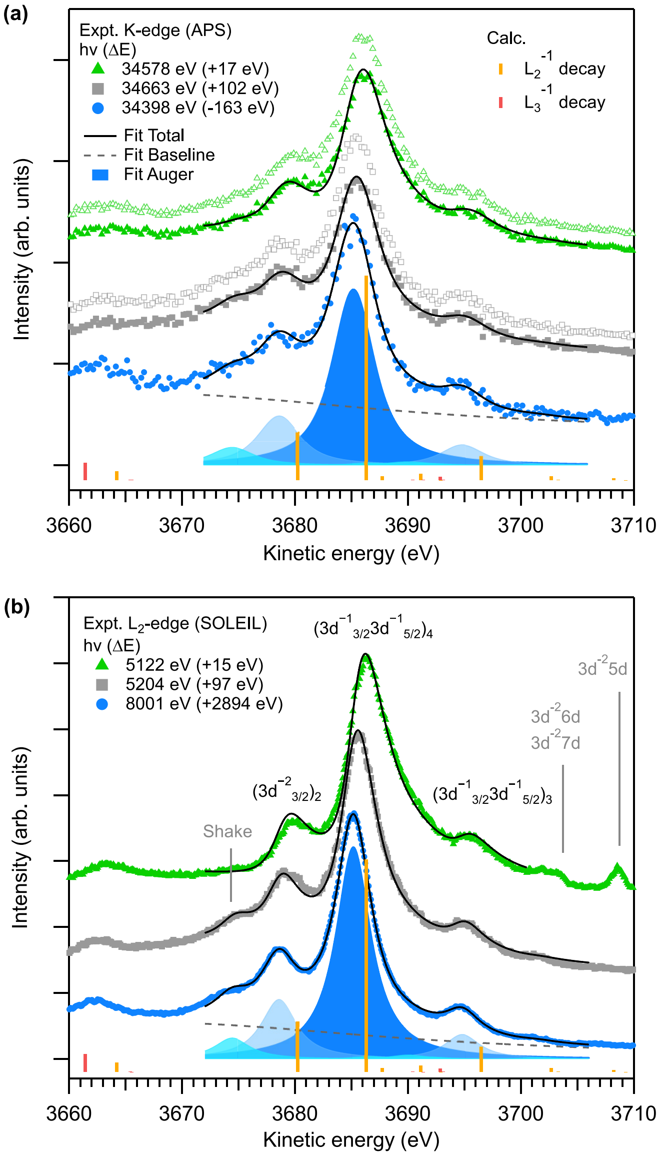

FIG. 2. Auger electron spectra measured (a) at the Xe *K* edge and (b) at the Xe L_2 edge. Three example spectra are shown from both experiments: one at a photon energy well above the L_2 edge yet below the *K* edge showing no PCI (blue), one at ∼15 eV excess energy (green), and one at ∼100 eV excess energy (gray). In (a), the open markers display the raw spectra, and the color-filled markers display the pure K-$L_2 \rightarrow L_2M_{4,5}M_{4,5}$ signal obtained by subtracting the underlying contribution from direct L_2-edge ionization (the below-*K*-edge reference). The spectra have been scaled to comparable height and offset vertically for clarity. The peak widths are governed by lifetime broadening; the estimated kinetic-energy resolution is 1.9 eV in all three *K*-edge spectra, 0.6 eV in the 8001-eV L_2-edge spectrum, and 0.4 eV in the 5122- and 5204-eV spectra. The bar spectra show calculated Auger line positions from Püttner *et al.* [16].

For the PCI analysis, we target the strong $(2p_{1/2}^{-1}) \rightarrow (3d_{3/2}^{-1}3d_{5/2}^{-1})_4$ Auger transition at ∼3685-eV kinetic energy [16], which was measured at a range of different photon energies around the *K* and L_2 edges. Here, the final state designation is jj-coupled $(nl_j^{-1}n'l'^{-1}_{j'})_J$ [16]. Figure 2(a) shows three example Auger spectra measured around the *K* edge: one below the *K* edge but well above the $L_{1,2,3}$ edges with no PCI (34 398 eV, blue), one slightly above the *K* edge with a strong PCI effect (34 578 eV, green), and one further above with a weaker PCI effect (34 663 eV, gray). In order to extract the pure K-$L_2 \rightarrow L_2M_{4,5}M_{4,5}$ signal from the *K*-edge measurements, the underlying contribution of $L_2M_{4,5}M_{4,5}$ decay from direct L_2 ionization has to be subtracted. This contribution is obtained from a below-*K*-edge reference measurement, which is the 34 398 eV trace shown in Fig. 2(a), and is assumed to have a constant yield (per measurement scan) over the probed photon-energy range; i.e., the direct L_2 photoionization cross section does not vary significantly in the covered *K*-edge region. In Fig. 2(a), the two spectra measured above the *K* edge are shown both before (above, open markers) and after (below, color-filled markers) subtracting the L_2 ionization contribution, with a small vertical offset for clarity. This subtraction step amounts to a relatively small correction (in terms of quantifying the PCI shift) in the above-threshold region where *K*-edge ionization dominates, as is seen from Fig. 2(a), but is more important at the onset of the threshold where the *K*-edge signal is still low in comparison. Calculated Auger spectra from Püttner *et al.* [16] are plotted as a bar spectrum for reference and indicate that the signals in this kinetic-energy range originate almost solely from the decay of L_2^{-1} states, with a few weak signatures from the decay of L_3^{-1} states and L_1^{-1} states contributing a practically negligible amount (see Ref. [16] for detailed assignments of the spectral lines). In Fig. 2(b), three spectra obtained around the L_2 edge are shown in a manner similar to that for the *K* edge in Fig. 2(a). Apart from the PCI effect, the overall spectral profiles plotted in Figs. 2(a) and 2(b) are seen to be rather similar at both edges. The small additional features seen in the 5122-eV spectrum in the 3700- to 3710-eV

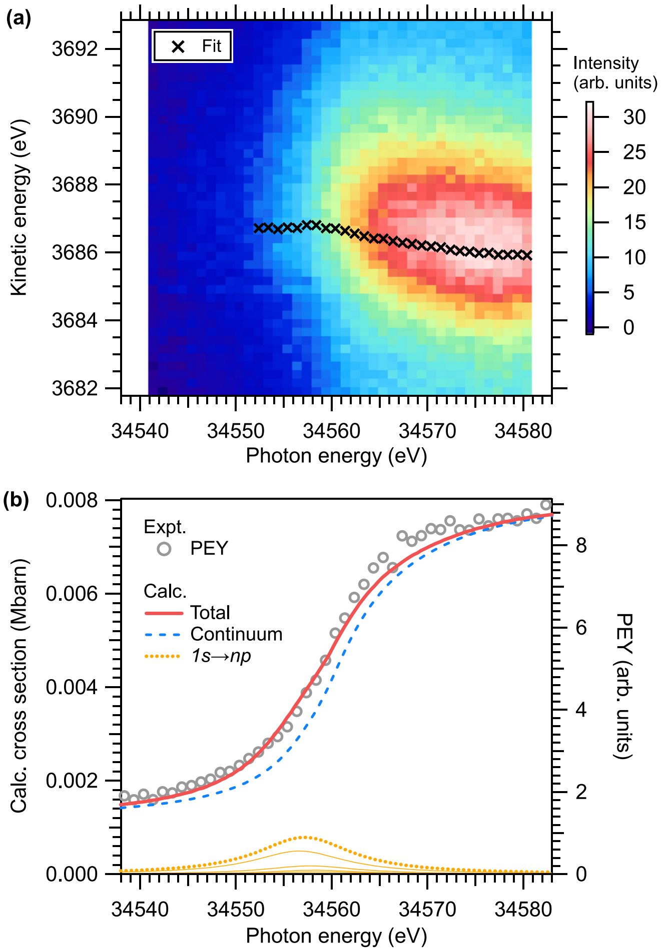

FIG. 3. (a) A 2D-map of Xe K-$L_2 \rightarrow L_2M_{4,5}M_{4,5}$ electron spectra measured as a function of the photon energy in the near-threshold region. The contribution from direct L-shell ionization has been subtracted from the data. The black markers indicate the fitted position of the transition to the $(3d_{3/2}^{-1}3d_{5/2}^{-1})_4$ state. (b) A partial-electron-yield (PEY) scan collecting electrons in the ~3342–3387-eV kinetic-energy range. A calculated absorption spectrum is shown for comparison, shifted by −88.1 eV to match the experiment.

kinetic-energy range correspond to resonant $2p^{-1} \rightarrow 3d^{-2}nd$ Auger transitions, which appear in the threshold region due to resonant-excitation and electron-recapture effects and disperse with photon energy [23]. Note that these lines are narrower than the normal Auger lines due to the resonant Raman effect [24]. This effect occurs due to energy-conservation arguments in first-step decays if the photon bandwidth is narrower than the lifetime broadening. In second-step decays like the resonant $2p^{-1}6p \rightarrow 3d^{-2}6p$ Auger decays subsequent to the $1s^{-1}6p \rightarrow 2p^{-1}6p$ x-ray emission (as discussed below in the context of Fig. 3), resonant Raman conditions are absent due to the balancing of the energy by the emission of the electron or photon in the first-step decay. One also observes that, in both Figs. 2(a) and 2(b), the low-excess-energy spectrum (green) has lower intensity on the lower-kinetic-energy side of the strongest Auger lines than seen in the two other spectra, which is particularly visible in the 3670- to 3680-eV kinetic-energy range. This should be due to Auger decay from shake-up and -off satellite states created in the photoionization step (as seen also in the $1s$ photoelectron spectrum in Fig. 1), which are not populated at low excess energies due to their higher energy thresholds and therefore contribute only at high excess energies [16].

From each spectrum, the PCI shift was quantified with a multi-peak fit employing PCI line shapes according to Eq. (12) from Van Der Straten *et al.* [6], with an emphasis on unified treatment of all spectra. Example fit results are included in Figs. 2(a) and 2(b). The most significant spectral contributions come from the $(2p_{1/2}^{-1}) \rightarrow (3d_{3/2}^{-1}3d_{5/2}^{-1})_4$ Auger transition at ~3685 eV, as well as from the nearby $(2p_{1/2}^{-1}) \rightarrow (3d_{3/2}^{-2})_2$ and $(2p_{1/2}^{-1}) \rightarrow (3d_{3/2}^{-1}3d_{5/2}^{-1})_3$ transitions at 3680 and 3696 eV, respectively. A number of weaker transitions centered within and slightly outside of this energy region were also included in the fit, as well as the satellite contribution mentioned above and a baseline curve. To guarantee systematic treatment, the same fixed relative PCI peak positions and relative intensities were applied for all of the fits at both edges. The fitting thus primarily focused on optimizing the absolute kinetic-energy positioning of the entire peak set. All PCI peaks were convoluted with fixed Gaussian widths based on the estimated analyzer base resolutions, and a fixed lifetime width (Γ parameter in the PCI line shape [6]) of 3.7 eV was applied for all spectra based on the experimental data. Overall, this treatment well reproduces the measured spectra, and it is emphasized that the primary focus here is on quantifying the PCI-induced kinetic-energy shifts, rather than finding the exact line shapes. A more detailed description of the applied fitting procedure is included in Appendix A.

Some further discussion of the Xe K-edge characteristics in the threshold region is warranted. In Fig. 3(a), we show a two-dimensional (2D) map of the Auger spectra measured near the threshold region at small photon-energy steps of 1 eV, with the electron kinetic energy on the vertical axis and photon energy on the horizontal axis. The direct L-shell ionization contribution has already been subtracted from this map. The markers in the image show the kinetic-energy position of the $(2p_{1/2}^{-1}) \rightarrow (3d_{3/2}^{-1}3d_{5/2}^{-1})_4$ line fitted with the procedure described above. In Fig. 3(b) a partial-electron-yield curve is shown for comparison, which was measured in a separate scan by collecting electrons from the strongest L_2-decay lines in the ~3342–3387-eV kinetic-energy range. Note that unlike in Fig. 3(a), L-shell contributions have not been subtracted from this curve; this, however, should lead only to a constant background. Additionally, a relativistic Hartree-Fock-Slater calculation [25] of the absorption spectrum is shown, including the continuum fraction and the Rydberg lines. To include the contribution from the dense Rydberg states with energy spacings less than their natural Lorentzian width, an arc tangent cross section model by Breinig *et al.* was used [26]. The calculated results have been shifted by −88.1 eV to match the experiment. In many previous experiments where maps similar to that shown in Fig. 3(a) have been measured for lighter elements, resonant excitations to unoccupied Rydberg orbitals were observed as distinct island structures, separate from the continuum fraction. This is also the case for the presently monitored decay lines when measured at the L_2 edge, where the $2p \rightarrow 5d$, $6d$, and $7d$ lines can be clearly identified [23].

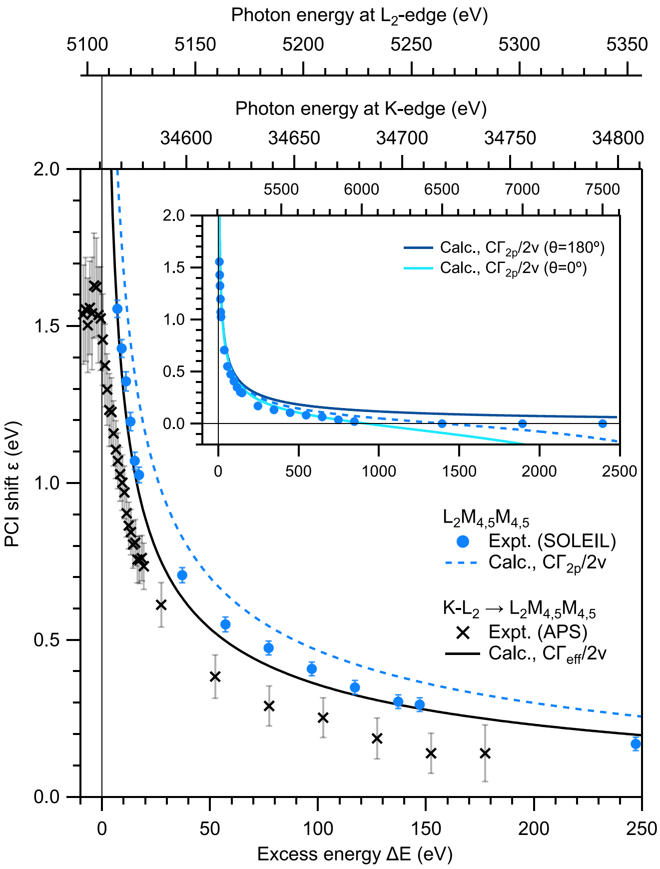

FIG. 4. PCI shift in K-$L_2 \rightarrow L_2M_{4,5}M_{4,5}$ decay near the K edge and in $L_2M_{4,5}M_{4,5}$ decay near the L_2 edge, as observed for the $(2p_{1/2}^{-1}) \rightarrow (3d_{3/2}^{-1}3d_{5/2}^{-1})_4$ transition. The markers display the experimental data. The lines show the calculated shifts according to Eq. (3). The inset shows data at the L_2 edge in a broader energy range and the calculated shifts for parallel ($\theta = 0^\circ$) and opposite ($\theta = 180^\circ$) electron ejections.

On the other hand, at the Xe K edge shown here, even the lowest-lying $1s \rightarrow 6p$ resonance is effectively drowned by the 10-eV-wide lifetime broadening to a quasicontinuous edge structure [27,28]. However, we may consider here that the position of the Rydberg resonance in the experiment corresponds to the photon energy (34 559 ± 2 eV) that produces the highest-kinetic-energy Auger electrons (see, e.g., [11,23]), which then also provides us with the nominal position of the IP (34 561 eV) because its relative shift from the Rydberg lines can be calculated from the optical data for Cs in the $Z + 1$ approximation. The lowest resonance ($1s \rightarrow 6p$) lies 2.46 eV below the ionization threshold [29], but based on the calculated effective profile that arises from the closely spaced lines [dotted line in Fig. 3(b)], we employ an effective shift of 1.94 eV. In the PCI analysis results presented below, the excess energy in the Xe K-edge data (in Fig. 4) is then calculated relative to the nominal IP determined this way. Note that the calibration accuracy of the photon energy in the absolute scale is a separate issue, as was noted above in Sec. II. Experimental values for the Xe($1s^{-1}$) binding energy were previously reported as 34 565.13 eV in Ref. [19] and 34 565 eV in Ref. [15], while theoretical values from recent high-level calculations were 34 563.6 eV in Ref. [15] and 34 563.7 eV in Ref. [30].

Figure 4 shows the main result of this work. The measured PCI-shift progressions at the K and L_2 edges are plotted as a function of the excess energy [the K-edge data shown here is the same as in Fig. 3(a), but here, additional data points at higher excess energies are shown at 25-eV steps]. For the K edge the excess energy is calculated as described in the paragraph above, and for the L_2 edge the IP value of 5106.72 eV reported in Ref. [19] is used as a reference. For both K and L_2 datasets the zero-PCI-shift position corresponds to the nominal kinetic energy measured at photon energies well above the L-edge (but below the K-edge) thresholds.

Comparing the two datasets in Fig. 4, it can be seen that the overall progressions are very similar at both edges. However, the data points suggest a systematic slightly reduced PCI shift at the K edge, which is in line with the additional x-ray emission step delaying the Auger emission in K-edge ionization and reducing the energy exchange. The difference between the two data series is subtle in comparison to the overall peak widths, although the gradual smooth progressions of the data points indicate that the fitting procedure is fairly robust, which should be due to the unified treatment of all spectra (Appendix A). The error bars in Fig. 4 account for the fit convergence within the given model parameters, including the determination of the reference kinetic energy without PCI and the effect of the experimental resolution. The error-estimation procedure is described in detail in Appendix B [Eq. (B1)], with additional discussion. The horizontal error in the excess energy should be comparable to the marker size and is therefore not plotted separately. Note that possible inaccuracy in the excess energy or in the reference kinetic-energy (no PCI) position would result in a small displacement of the entire data series, rather than varying the data points individually.

For comparison with the experiment, we also calculate the PCI shifts ε using the simple expression

$$\varepsilon = \frac{C\Gamma}{2v_1}, \tag{3}$$

which derives from a semiclassical formulation described by Van Der Straten *et al.* [6] [their Eq. (13)]. Note that the same formulation was used in fitting the experimental PCI line shapes (Appendix A). Here, $C = 1 - v_1/(|\mathbf{v_2} - \mathbf{v_1}|)$, where $\mathbf{v_1}$ and $\mathbf{v_2}$ are the velocities of the slower and faster electrons, respectively [6]. At the L_2 edge, Γ corresponds to the $2p^{-1}$ lifetime width Γ_{2p}. At the K edge, the lifetime of the $1s^{-1}$ state must also be considered, with the x-ray-emission step delaying the PCI effect. By simply taking the sum of the $1s^{-1}$ and $2p^{-1}$ lifetimes, an "effective decay width" can be calculated as $\Gamma_{\text{eff}} = \Gamma_{1s}\Gamma_{2p}/(\Gamma_{1s} + \Gamma_{2p})$, similar to that in earlier works [9,11,12,31]. Employing the values $\Gamma_{2p} = 3.04$ eV [32] and $\Gamma_{1s} = 10.0$ eV, corresponding to $\Gamma_{\text{eff}} = 2.33$ eV for the K edge, PCI-shift curves calculated with Eq. (3) are plotted in Fig. 4. It is seen that this relatively simple model finds fairly good agreement with the experimental data. The difference between the calculated curves for the K and L_2 edges is comparable to that observed in the experiment. The C parameter in Eq. (3) has only marginal dependence on the vector relation (emission angle θ between the two electrons) in the excess-energy range of interest (<250 eV), which is clear from the inset in Fig. 4, where we show a broader energy range view of the L_2-edge data and plot the calculation for parallel and opposite ejections separately (see Eq. (17) in Ref. [6]). Therefore, we have omitted consideration of the angular distributions and simply applied the average of parallel and opposite ejections for the curves plotted in the main part of the figure.

IV. CONCLUSIONS

Using electron spectroscopy at two synchrotron facilities, we examined the x-ray-fluorescence delay effect on PCI shifts between Xe K-$L_2 \rightarrow L_2M_{4,5}M_{4,5}$ and $L_2M_{4,5}M_{4,5}$ decay spectra upon hard-x-ray photoionization at the Xe K and L_2 edges, respectively. With similar studies carried out previously at the Ar and Kr K edges [9–14], the present work extends understanding of the phenomenon to the deep Xe K edge. Overall, the PCI-shift progressions were observed to be relatively similar at both Xe K and L_2 edges. However, the data indicate a small but systematic decrease in the PCI shift at the K edge, which can be attributed to the few-attosecond τ_{1s} lifetime of the deep Xe($1s^{-1}$) core hole extending the effective lifetime by ∼30% compared to τ_{2p}. The experiment is in reasonable quantitative agreement with predictions from a semiclassical theoretical model [6]. Discussion of the Xe 1s photoelectron and absorption spectra was also provided in relation to the photoionization dynamics, the effect of the ultrashort core-hole lifetime, and energy calibration at the Xe K edge; the strong lifetime broadening of deep core-hole states such as Xe($1s^{-1}$) clearly complicates accurate interpretation of the near-threshold interaction and the photoelectron spectrum, in comparison to lower edges. In this context, state-selective multicoincidence methods [9,10,13] or alternative approaches may turn out to be beneficial.

ACKNOWLEDGMENTS

This work was supported by the U.S. Department of Energy, Office of Science, Basic Energy Sciences, Chemical Sciences, Geosciences, and Biosciences Division. This research used resources of the Advanced Photon Source, a U.S. Department of Energy (DOE) Office of Science User Facility operated for the DOE Office of Science by Argonne National Laboratory under Contract No. DE-AC02-06CH11357. Experiments were also performed on the GALAXIES beamline at SOLEIL Synchrotron, France (Project No. 99230023). We are grateful to the APS and SOLEIL staff for their smooth operation of the facilities. We thank R. Dejus from the Advanced Photon Source for helpful discussions regarding the undulator divergence and bandwidth estimation. N.V. and T.M. acknowledge funding from the European Union's Horizon 2020 research and innovation program under Marie Skłodowska-Curie Grant Agreement No. 860553.

APPENDIX A: FITTING PROCEDURE

The multipeak fits were performed using the curve_fit least-squares optimization function included in the PYTHON library SCIPY (version 1.11.2) [33]. For all K-edge spectra, apart from the below-threshold reference, the L-edge contribution was subtracted before the fitting, as discussed in the main text. The applied PCI line shapes follow Eq. (12) in Ref. [6] and were additionally convoluted with Gaussians to account for the experimental resolution. The Gaussian FWHM was fixed to 1.9 eV in the K-edge spectra or to 0.4 eV (for $h\nu < 6\,\mathrm{keV}$) or 0.6 eV (for $h\nu > 6\,\mathrm{keV}$) in the L_2-edge spectra. These values were calculated according to $E_P w/(2R)$, where E_P is the pass energy, w is the slit width, and R is the analyzer radius. Γ was fixed to 3.7 eV for all PCI peaks in all spectra at both edges based on the experimental data, which is fairly close to the estimate of 4.0 eV obtained by summing the 3.04-eV [32] initial-state ($2p^{-1}$) width and 1.0-eV final-state ($3d^{-2}$) width (the latter is approximated by taking twice the 0.5-eV ($3d^{-1}$) state width [34]). (Note that for a more exact description of the line shape one has to use a more complex approach, namely, a PCI line shape with the width of the lifetime broadening of the initial state convoluted with a Lorentzian with the width of the lifetime broadening of the final state, along with a Gaussian accounting for the experimental resolution; see, e.g., Ref. [8].)

TABLE I. Relative kinetic-energy positions and intensities of the PCI line shapes applied in fitting the Auger spectra. The energy E and intensity parameters (I and I') were fitted as described in the text. The assignments are from Ref. [16].

Peak	Assignment	Energy (eV)	Intensity
1	$2p_{3/2}^{-1} \rightarrow (3p_{3/2}^{-1}4p_{3/2}^{-1})_2$	$E - 23.13$	$0.064I$
2	Shake	$E - 10.73$	I'
3	$2p_{1/2}^{-1} \rightarrow (3d_{3/2}^{-1}3d_{5/2}^{-1})_4$	E	I
4	$2p_{1/2}^{-1} \rightarrow (3d_{3/2}^{-2})_2$	$E - 6.60$	$0.280I$
5	$2p_{1/2}^{-1} \rightarrow (3d_{3/2}^{-1}3d_{5/2}^{-1})_3$	$E + 9.64$	$0.115I$
6	$2p_{1/2}^{-1} \rightarrow (3d_{3/2}^{-1}3d_{5/2}^{-1})_1$	$E + 1.44$	$0.012I$
7	$2p_{1/2}^{-1} \rightarrow (3d_{3/2}^{-1}3d_{5/2}^{-1})_2$	$E + 4.83$	$0.019I$
8	$2p_{3/2}^{-1} \rightarrow (3p_{1/2}^{-1}4d_{5/2}^{-1})_3$	$E + 6.56$	$0.010I$
9	$2p_{1/2}^{-1} \rightarrow (3d_{5/2}^{-2})_2$	$E + 16.39$	$0.007I$

The relative kinetic-energy positions and relative intensities of the PCI peaks were fixed according to Table I at both edges. These relations were optimized based on initial free parameter fits to the experimental data, as well as in reference to the calculation (regarding the weaker transitions in particular) [16]. The peak assignments given in Table I are from Püttner *et al.* [16] (see the strongly contributing transitions presented in their Supplemental Material). The reference Auger kinetic energy E_0 was first determined from spectra where PCI was negligible with symmetric line shapes (see Appendix B). Note that this value is the same for both edges by definition (applying a common kinetic-energy-scale calibration). This value was then fixed for all other spectra subject to PCI, and the line shape was allowed to vary only via the C/v_1 parameter (see [6]) by leaving the nominal excess energy (and therefore v_1) free to be optimized by the fit. This means that the effective peak position (PCI shift) and peak asymmetry are linked via a common fit parameter and not allowed to vary independently, which unifies the treatment of all spectra. The effective peak position is then $E = E_0 + \varepsilon$, where the PCI shift ε obeys Eq. (3); it is emphasized that while in the final paragraph of Sec. III this expression was used for directly calculating the PCI shift (line traces in Fig. 4), here, the overall formulation is instead used for fitting the experimental line shapes. The spectral intensity I was left as a free fit parameter. The shake peak intensity I' was separately left free as it varies between some of the spectra. The background was described with a constant plus a broad Lorentzian shape (fixed at 3667-eV kinetic energy, with 26-eV FWHM), the intensities of which were also free parameters; the purpose of the Lorentzian is to mimic the overall nonconstant background profile around this energy region (see, e.g., Ref. [16] for a broader-energy-range view). Appropriate constraints were applied, including allowing only positive PCI peak intensities and asymmetries. The fitted kinetic-energy range was 3672–3706 eV for all spectra, apart from the low photon energies ($h\nu < 5125$ eV) at the L_2 edge where the range was restricted to exclude overlapping resonant Auger features from the fit (see Fig. 2). Uncertainties for the individual data points were not specified in the model optimization.

APPENDIX B: ERROR ESTIMATION

The error bars in Fig. 4 are calculated by combining different potential sources of error. First, standard-deviation error estimates of the optimal fit parameters are obtained for each spectrum from the applied curve_fit PYTHON function [33]. We take the evaluated errors for the kinetic-energy positions multiplied by 2 for higher confidence, denoting them ΔE_{FIT}. Second, the reference Auger energy position (with respect to which the PCI shifts are calculated) has its own uncertainty, denoted ΔE_{REF}. For the L_2 edge, we apply the mean fitted kinetic energy from five separate measurements taken at photon energies well above the IP ($h\nu = 7$–$10\,\mathrm{keV}$) and calculate its error as $\Sigma \Delta E_i/\sqrt{5}$, where ΔE_i are the individual fitting errors (defined as above). For the K-edge data, one reference measurement was taken at $h\nu = 34.4\,\mathrm{keV}$, from which we take the fitted kinetic energy and its respective fitting error. Third, uncertainty in the applied Gaussian widths (experimental resolution) will also have a small influence on the effective PCI shifts [6]. This is more relevant for the K-edge data than the L_2-edge data due to the poorer experimental resolution in the former. An exact uncertainty estimate for the experimental resolution cannot be provided, but we apply a conservative number to account for this sensitivity. We reperformed the K-edge fits upon varying the Gaussian FWHM by ±1.0 eV, and the resulting changes in the PCI shifts were applied as an additional error contribution ΔE_{RES}. Note that while the effective peak positions seen in the experiment have a slight dependence on Gaussian broadening [6], in this work we report the true ("deconvoluted") peak positions extracted from the fit. Combining the above, the total error ΔE_{PCI} is then calculated as

$$\Delta E_{\mathrm{PCI}} = \sqrt{\Delta E_{\mathrm{FIT}}^2 + \Delta E_{\mathrm{REF}}^2 + \Delta E_{\mathrm{RES}}^2}, \tag{B1}$$

with the third term applying only to the K-edge data. The relative importance of the three contributions varies; ΔE_{FIT} and ΔE_{RES} have a decreasing trend with increasing excess energy, but close to the threshold they are comparable to or higher than ΔE_{REF} (which stays constant). The absolute precisions of the data points are naturally also subject to the uncertainties of the rest of the model parameters, but as they are fixed and common for both datasets (except for the background and shake intensities), we omit their consideration.

At the K edge, the subtraction of the underlying direct L ionization contribution poses another potential source of error. This is not accounted for in the error bars of Fig. 4, but to quantify the effect of this analysis step, the K-edge fits were also performed without subtracting the L-edge contribution. The PCI shifts turn out to be slightly smaller than presented in Fig. 4, e.g., by −0.25 eV at the threshold, by −0.11 eV at 10-eV excess energy, and by −0.02 eV at 102-eV excess energy. The data points close to the ionization threshold are thus noticeably changed by the subtraction, but small uncertainty in this step alone would be unlikely to explain the observed difference between the two edges.

[1] V. Schmidt, N. Sandner, W. Mehlhorn, M. Y. Adam, and F. Wuilleumier, Post-collision interaction in the xenon $N_{4,5}$-OO Auger spectrum excited by photon impact, Phys. Rev. Lett. **38**, 63 (1977).

[2] M. U. Kuchiev and S. A. Sheĭnerman, Post-collision interaction in atomic processes, Sov. Phys. Usp. **32**, 569 (1989).

[3] G. B. Armen, J. Tulkki, T. Aberg, and B. Crasemann, Quantum theory of post-collision interaction in inner-shell photoionization: Final-state interaction between two continuum electrons, Phys. Rev. A **36**, 5606 (1987).

[4] A. Niehaus, Analysis of post-collision interactions in Auger processes following near-threshold inner-shell photoionization, J. Phys. B **10**, 1845 (1977).

[5] A. Russek and W. Mehlhorn, Post-collision interaction and the Auger lineshape, J. Phys. B **19**, 911 (1986).

[6] P. Van der Straten, R. Morgenstern, and A. Niehaus, Angular dependent post-collision interaction in Auger processes, Z. Phys. D **8**, 35 (1988).

[7] W. Eberhardt, S. Bernstorff, H. W. Jochims, S. B. Whitfield, and B. Crasemann, Photoelectron recapture through post-collision interaction, Phys. Rev. A **38**, 3808 (1988).

[8] R. Guillemin, S. Sheinerman, R. Püttner, T. Marchenko, G. Goldsztejn, L. Journel, R. K. Kushawaha, D. Céolin, M. N. Piancastelli, and M. Simon, Postcollision interaction effects in *KLL* Auger spectra following argon 1*s* photoionization, Phys. Rev. A **92**, 012503 (2015).

[9] R. Guillemin, S. Sheinerman, C. Bomme, L. Journel, T. Marin, T. Marchenko, R. K. Kushawaha, N. Trcera, M. N. Piancastelli, and M. Simon, Ultrafast dynamics in post-collision interaction after multiple Auger decays in argon 1*s* photoionization, Phys. Rev. Lett. **109**, 013001 (2012).

[10] L. Gerchikov, P. Lablanquie, J. Palaudoux, F. Penent, and S. Sheinerman, Postcollision interaction in sequential x-ray radiative and Auger decays after atomic inner-shell photoionization, Phys. Rev. A **107**, 062822 (2023).

[11] S. Kosugi, R. Guillemin, O. Travnikova, T. Marchenko, D. Koulentianos, J. B. Martins, F. Hosseini, R. Püttner, D. Céolin, L. Journel, M. N. Piancastelli, I. Ismail, F. Koike, M. Iizawa, S. Sheinerman, L. Gerchikov, Y. Azuma, and M. Simon, Postcollision-interaction effects in multistep Auger transitions following Ar 1*s* photoionization, Phys. Rev. A **106**, 033114 (2022).

[12] S. Li, D. Koulentianos, S. H. Southworth, G. Doumy, L. Young, D. A. Walko, R. Püttner, J. D. Bozek, D. Céolin, A. Verma, R. Guillemin, M. N. Piancastelli, M. Simon, L. G. Gerchikov, and S. A. Sheinerman, Manifestation of postcollision interaction in Krypton *LMN* Auger spectra following *K*-shell photoionization, Phys. Rev. A **106**, 023110 (2022).

[13] U. Arp, T. LeBrun, S. H. Southworth, M. A. MacDonald, and M. Jung, X-ray fluorescence and Auger-electron coincidence spectroscopy of vacancy cascades in atomic argon, Phys. Rev. A **55**, 4273 (1997).

[14] S. Kosugi, F. Koike, M. Iizawa, M. Oura, T. Gejo, K. Tamasaku, J. R. Harries, R. Guillemin, M. N. Piancastelli, M. Simon, and Y. Azuma, Fluorescence time delay in multistep Auger decay as an internal clock, Phys. Rev. Lett. **124**, 183001 (2020).

[15] M. N. Piancastelli, K. Jänkälä, L. Journel, T. Gejo, Y. Kohmura, M. Huttula, M. Simon, and M. Oura, X-ray versus Auger emission following Xe 1*s* photoionization, Phys. Rev. A **95**, 061402(R) (2017).

[16] R. Püttner, K. Jänkälä, R. K. Kushawaha, T. Marchenko, G. Goldsztejn, O. Travnikova, R. Guillemin, L. Journel, I. Ismail, B. Cunha de Miranda, A. F. Lago, D. Céolin, M. N. Piancastelli, and M. Simon, Detailed assignment of normal and resonant Auger spectra of Xe near the *L* edges, Phys. Rev. A **96**, 022501 (2017).

[17] D. A. Walko, B. W. Adams, G. Doumy, E. M. Dufresne, Y. Li, A. M. March, A. R. Sandy, J. Wang, H. Wen, and Y. Zhu, Developments in time-resolved x-ray research at APS beamline 7ID, in *Proceedings of the 12th International Conference on Synchrotron Radiation Instrumentation–SRI2015*, edited by Q. Shen and C. Nelson, AIP Conf. Proc. No. 1741 (AIP, New York, 2016), p. 030048.

[18] D. Céolin, J. Ablett, D. Prieur, T. Moreno, J.-P. Rueff, T. Marchenko, L. Journel, R. Guillemin, B. Pilette, T. Marin, and M. Simon, Hard X-ray photoelectron spectroscopy on the GALAXIES beamline at the SOLEIL synchrotron, J. Electron Spectrosc. Relat. Phenom. **190**, 188 (2013).

[19] R. D. Deslattes, E. G. Kessler, P. Indelicato, L. de Billy, E. Lindroth, and J. Anton, X-ray transition energies: New approach to a comprehensive evaluation, Rev. Mod. Phys. **75**, 35 (2003).

[20] M. Oura, T. Gejo, K. Nagaya, Y. Kohmura, K. Tamasaku, L. Journel, M. N. Piancastelli, and M. Simon, Hard x-ray photoelectron spectroscopy on heavy atoms and heavy-element containing molecules using synchrotron radiation up to 35 keV at SPring-8 undulator beamlines, New J. Phys. **21**, 043015 (2019).

[21] S. H. Southworth, T. LeBrun, Y. Azuma, and K. G. Dyall, Argon KM photoelectron satellites, J. Electron Spectrosc. Relat. Phenom. **94**, 33 (1998).

[22] R. Püttner, P. Holzhey, M. Hrast, M. Žitnik, G. Goldsztejn, T. Marchenko, R. Guillemin, L. Journel, D. Koulentianos, O. Travnikova, M. Zmerli, D. Céolin, Y. Azuma, S. Kosugi, A. F. Lago, M. N. Piancastelli, and M. Simon, Argon *KLL* Auger spectrum: Initial states, core-hole lifetimes, shake, and knock-down processes, Phys. Rev. A **102**, 052832 (2020).

[23] R. K. Kushawaha, K. Jänkälä, T. Marchenko, G. Goldsztejn, R. Guillemin, L. Journel, D. Céolin, J.-P. Rueff, A. F. Lago, R. Püttner, M. N. Piancastelli, and M. Simon, Auger resonant-Raman decay after Xe *L*-edge photoexcitation, Phys. Rev. A **92**, 013427 (2015).

[24] M. Piancastelli, Auger resonant raman studies of atoms and molecules, J. Electron Spectrosc. Relat. Phenom. **107**, 1 (2000).

[25] A. E. A. Fouda, P. J. Ho, R. W. Dunford, E. P. Kanter, B. Krässig, L. Young, E. R. Peterson, E. C. Landahl, L. Pan, D. R. Beck, and S. H. Southworth, Resonant x-ray absorption of strong-field-ionized CF_3Br, J. Phys. B **53**, 244009 (2020).

[26] M. Breinig, M. H. Chen, G. E. Ice, F. Parente, B. Crasemann, and G. S. Brown, Atomic inner-shell level energies determined by absorption spectrometry with synchrotron radiation, Phys. Rev. A **22**, 520 (1980).

[27] M. Deutsch and P. Kizler, X-ray multielectronic photoexcitations near the *K* edge of xenon, Phys. Rev. A **45**, 2112 (1992).

[28] C. M. Teodorescu, R. C. Karnatak, J. M. Esteva, A. E. Afif, and J. P. Connerade, Unresolvable Rydberg lines in x-ray absorption spectra of free atoms, J. Phys. B **26**, 4019 (1993).

[29] A. Kramida, Yu. Ralchenko, J. Reader, and NIST ASD Team, NIST Atomic Spectra Database, version 5.10, https://physics.nist.gov/asd, and references therein.

[30] S. H. Southworth, R. W. Dunford, D. Ray, E. P. Kanter, G. Doumy, A. M. March, P. J. Ho, B. Krässig, Y. Gao, C. S. Lehmann, A. Picón, L. Young, D. A. Walko, and L. Cheng, Observing pre-edge *K*-shell resonances in Kr, Xe, and XeF_2, Phys. Rev. A **100**, 022507 (2019).

[31] C. Bomme, R. Guillemin, S. Sheinerman, T. Marin, L. Journel, T. Marchenko, R. Kushawaha, N. Trcera, M. N. Piancastelli, and M. Simon, Post-collision interaction manifestation in molecular systems probed by photoelectron-molecular ion coincidences, J. Phys. B **46**, 215101 (2013).

[32] J. Campbell and T. Papp, Widths of the atomic K–N7 levels, At. Data Nucl. Data Tables **77**, 1 (2001).

[33] P. Virtanen *et al.*, Scipy 1.0: Fundamental algorithms for scientific computing in python, Nat. Methods **17**, 261 (2020).

[34] M. Jurvansuu, A. Kivimäki, and S. Aksela, Inherent lifetime widths of Ar $2p^{-1}$, Kr $3d^{-1}$, Xe $3d^{-1}$, and Xe $4d^{-1}$ states, Phys. Rev. A **64**, 012502 (2001).